RSC Advances

PAPER

View Article Online
View Journal | View Issue

Cite this: *RSC Adv.*, 2021, **11**, 21767

Study of charge transfer mechanism and dielectric relaxation of all-inorganic perovskite $CsSnCl_3$

Mohamed Ben Bechir *[a] and Mohamed Houcine Dhaou[b]

Received 28th March 2021
Accepted 13th June 2021

DOI: 10.1039/d1ra02457d

rsc.li/rsc-advances

In the field of commercialization, lead-free metal halide perovskite materials are becoming more popular these days because of their prospective use in solar cells and also in other optoelectronic applications. In this paper, a non-toxic $CsSnCl_3$ metal halide is successfully synthesized *via* the slow evaporation solution growth technique. Such systematic characterizations as differential scanning calorimetry (DSC) measurements, dielectric measurements, and variable-temperature structural analyses indicate that $CsSnCl_3$ goes through a reversible phase transformation at $T = 391/393$ K from the monoclinic to the cubic system. Optical measurements of $CsSnCl_3$ reveal a direct band-gap value of about 3.04 eV. The study of the charge transfer mechanism of $CsSnCl_3$ is carried out based on Elliott's theory. The conduction mechanism in $CsSnCl_3$ is interpreted through the following two approaches: the non-overlapping small polaron tunneling (NSPT) model (monoclinic phase) and the overlapping large polaron tunneling (OLPT) model (cubic phase). Moreover, the high dielectric constant of $CsSnCl_3$ which is associated with a low dielectric loss makes it a possible candidate for energy harvesting devices.

1. Introduction

Metal halide perovskite materials of the well-known formula AMX_3 (where A = a cation, M = a metal ion, and X = a halogen anion) have recently attracted researchers' attention owing to their marked solar cell potency with astonishing optoelectronic proprieties including a vast range of absorption spectra, improved optical absorption, tunable bandgap, high charge-carrier mobility and low effective mass.[1–3] The researchers have started the application of these semiconducting materials which are also widespread in the field of such electronic devices as LEDs (Light Emitting Diodes) and photodetectors, and the devices that are largely employed for solar-to-fuel energy conversion.[4–6] In addition, these metal halide perovskites are inexpensive and widely available on Earth. As a consequence, these semiconductors would be more appropriate and favorable to the solar cell application relative to the Si-based photovoltaic (PV) technology.[3] Nevertheless, most of the halide perovskites with superlative properties are composed of lead (Pb) which has a damaging effect on the environment.[7–9] Eco-friendly energy sources have caught much attention because of environmental contamination and the global energy crisis. Hence, a big number of experimental and theoretical works have been carried out in the last few years to replace Pb with a convenient metal cation.[10–13] In the perovskite structure, using Sn^{2+} instead of Pb^{2+} removes the toxicity of the halide inorganic material but provides more pronounced phase instability.

Furthermore, The CsSnX3 compounds are direct bandgap semiconductors with good hole mobilities. Moreover, these Metal halide perovskite materials have small excitation binding energies, high values of the optical absorption coefficient, and the range of bandgap values was 1–3 eV.[14,15] All these properties make the CsSnX3 compounds promising candidates for opto-electronic nanodevices. Lately, solar cells using CsSnX3 have been made, and until now the maximum power conversion efficiency (PCE) is up to 9.13% (CsSnBr3 based device).[16–18] In addition to the application in PV, the important physical properties of $CsSnX_3$ also enable these compounds to be good for different applications, such as ferroelectricity, photo-luminescence, and X-ray detectors. Hao *et al.* have noted that the $CsSnI_3$ compound had important photoluminescence characteristics, and the tunable photoluminescence covered the whole visible to the near-infrared zone.[19,20]

This paper focuses on $CsSnCl_3$, a comparatively stable but less studied member of the $CsSnX_3$ family. Nonetheless, extensive investigations on its structural and dielectric properties are very important to evaluate the compatibility of inorganic materials with the field of next-generation photovoltaics and optoelectronics. Multiple researchers have concentrated on the synthesis and optical/optoelectronic characterization of metal halide perovskite materials[21] through which charge transport plays a key role in the efficiency of the electrical and the opto-electronic devices. Nonetheless, a thorough knowledge of the electrical transport mechanism is still missing along with the dielectric behavior of $CsSnCl_3$.[22]

[a]*Laboratory of Spectroscopic and Optical Characterization of Materials (LaSCOM), Faculty of Sciences, University of Sfax, BP1171 – 3000, Sfax, Tunisia. E-mail: mohamedbenbechir@hotmail.com*

[b]*Department of Physics College of Science Qassim University, Buraydah, Almolaydah, 51452-P.O.Box: 6644, Saudi Arabia*

Dielectric spectroscopy is broadly employed to gather information on the AC conduction mechanism and dielectric relaxation in a vast frequency range of different temperatures. The dielectric properties can be examined by establishing multiple parametric tools such as complex impedance, dielectric permittivity, electrical modulus, and also AC conductivity. The qualitative representation frequently provides the latest insight into the field of dielectric behavior. In the material, non-localized (known as long-range conductivity) and localized conduction (also known as dielectric relaxation) processes can, for instance, be marked by either the absence or the presence of the relaxation peak from the imaginary modulus plots. Specific transport mechanism can be defined using the activation energy and the relaxation time for material. The behavior of the dielectric parameter was previously investigated on perovskite oxide materials, amorphous transition metal oxide semiconductors, ionically conducting polymers, and conducting glasses.[23–25]

The synthesis is reported in this paper along with the structural and optical characterization of $CsSnCl_3$. This paper offers an in-depth investigation of dielectric and electrical properties as this perovskite is relatively unexplored. Impedance spectroscopy is a very suitable and practical tool to research dielectric properties. The temperature and frequency-dependent dielectric study of $CsSnCl_3$ can give in-depth information concerning the performance of the localized charge carriers, conduction mechanism, permittivity, loss factor, *etc.* Very little literature about the extensive research on AC conductivity, and dielectric relaxation of $CsSnCl_3$ is available. In this paper, the study of dielectric relaxation with impedance spectroscopy, electrical modulus and conductivity of $CsSnCl_3$ has been thoroughly conducted as a function of frequency and temperature. Using different theoretical models, the results of the dielectric researches have been carefully scrutinized. In-depth discussions on the AC and DC conductivity, dielectric loss, dielectric constant, impedance study, and also electrical modulus of this perovskite material are reported in this paper.

2. Experimental section

2.1. Materials

Cesium chloride (Sigma-Aldrich, ≥98.0%) and Tin(II) chloride (Sigma-Aldrich, reagent grade, 98%) were employed as received without further purification.

2.2. Synthesis

The $CsSnCl_3$ compound was synthesized by the evaporation at room temperature method with stoichiometric quantities of CsCl (0.94 g, 0.0055 mol) and $SnCl_2$ (1.05 g, 0.0055 mol) in deionized water (50 mL) according to the following equation:

$$CsCl + SnCl_2 \rightarrow CsSnCl_3$$

The solution obtained was slowly evaporated at room temperature. The product was purified by different successive recrystallizations. Throughout these steps, the crystal quality improved, and transparent single crystals of $CsSnCl_3$ were obtained and chosen for further experiments.

2.3. Characterization

The differential scanning calorimetric study (DSC) was carried out on a Perkin-Elmer Diamond DSC apparatus in the temperature range of 300–500 K with a rate of 5 K min^{-1} under a nitrogen (N_2) atmosphere.

A small quantity of $CsSnCl_3$ crystals was ground mechanically in an agate mortar with a pestle to obtain fine powders so as the powder X-ray diffraction (PXRD). The PXRD analysis was conducted by means of a Rigaku MiniFlex 600 benchtop diffractometer using a Cu K_α line radiation ($\lambda = 1.54$ Å) in the $2\theta = 10°$–$60°$ range with a 0.04° step size at 303 and 403 K.

Thermogravimetric (TG) analysis was done at a range of heating rates from 300 to 900 K with a Perkin Elmer Pyris 6 in a closed perforated aluminum pan under an N_2 gas flow. The TG analysis was made on powder from the obtained $CsSnCl_3$ crystals.

Ultraviolet-visible diffuse reflectance measurement was conducted on a PerkinElmer Lambda 950 UV-Vis spectrophotometer, whereas the UV-Vis absorption spectrum was carried out on a single crystal of the material at room temperature.

A small quantity of $CsSnCl_3$ crystals was ground mechanically in an agate mortar with a pestle to obtain fine powders so as to measure the complex impedance. $CsSnCl_3$ pellet (0.93 mm thickness) was prepared under a nitrogen (N_2) atmosphere (at room temperature) with a hydraulic press of 8 mm diameter under a 50 Torr pressure, and the relative density was found to be equal to 93%. The resulting pellet was put between two copper electrodes. In order to make good electrical contact between the sample and the electrodes, the pellet was coated with silver paint. AC conductivity and dielectric relaxation were investigated by the TH2828A impedance analyzer (frequency range 10^{-1}–10^6 Hz) associated with a temperature controller (TP94, Linkam, Surrey, UK) from 303 K to 483 K at a heating rate of 2 K min^{-1}. The measured AC voltage was 0.5 V.

3. Results and discussion

3.1. Temperature-dependent structural analysis

The DSC measurement of both heating and cooling is an effective way to measure the temperature-triggered phase transition. The DSC curve for $CsSnCl_3$ demonstrates an endothermic peak which takes place at 393 K and also an exothermic peak found at 391 K as shown in Fig. 1(a). The sharp reversible peaks confirm that they ought to be first-order phase transitions. The phase transition at $T = 391/392$ K is confirmed by the PXRD pattern at 303 and 403 K (Fig. 1(b)).

The crystal structure of $CsSnCl_3$ was obtained at 303 K using powder X-ray diffraction. The diffractogram is shown in Fig. 1(b). All the peaks seen in this diffractogram were indexed with the Celeref. 3 software by the least square method from the powder data.[26] The PXRD pattern proves that $CsSnCl_3$ crystallizes at 303 K in the monoclinic system with the space group $P2_1/n$ and has the unit cell parameters $a = 16.089$ (2) Å, $b =$

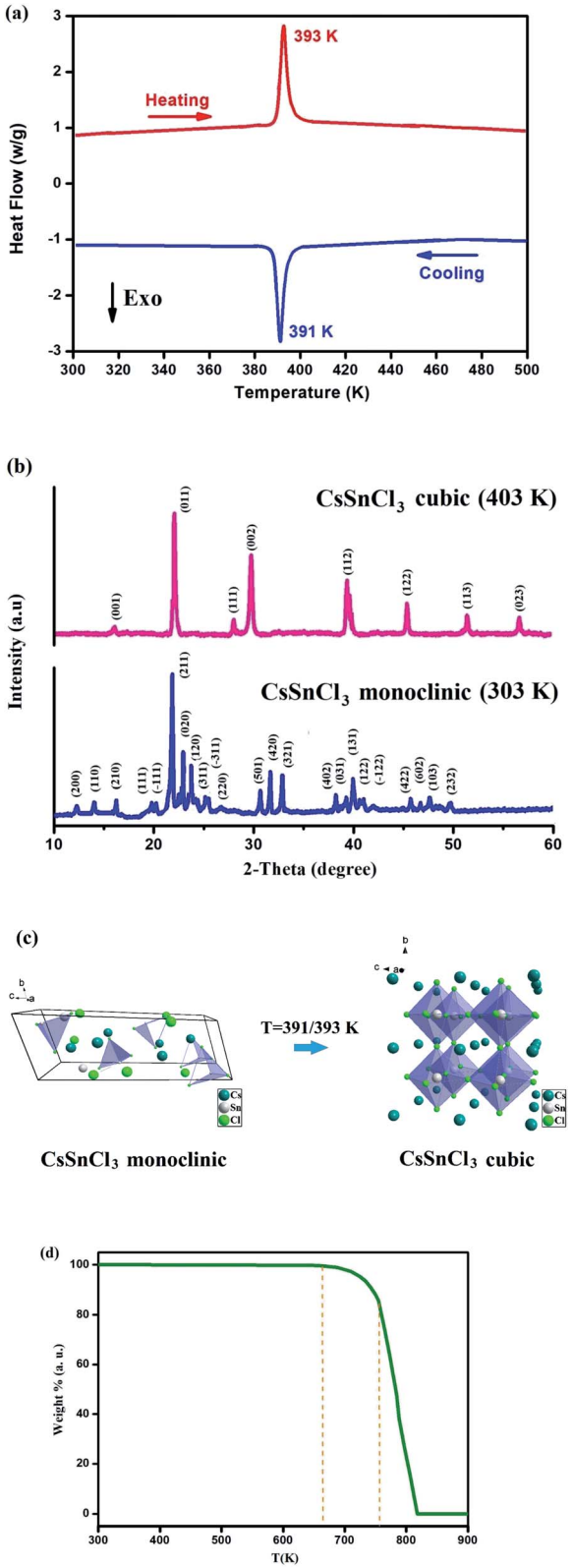

Fig. 1 (a) DSC curves of $CsSnCl_3$. (b) PXRD patterns of $CsSnCl_3$ at 303 and 403 K. (c) Constructed monoclinic and cubic structures of $CsSnCl_3$. The crystal structures were designed using VESTA. (d) TG curve of $CsSnCl_3$ in the temperature range of 300–900 K.

7.419 (5) Å, c = 5.739 (4) Å and $\beta = 93.4°$. On the other hand, $CsSnCl_3$ crystallizes at 403 K in the cubic system with the space group $Pm\bar{3}m$ and the refined unit-cell parameters: a = 5.579 (3) Å, and V = 173.64 (Å^3). The parameters values found in both phases are in accord with the values of the literature.[27,28]

As indicated in Fig. 1(c), the molecular structure of $CsSnCl_3$ for the two alternative phases (monoclinic and cubic) is obtained by the Vesta software. The thermogravimetric analysis data of $CsSnCl_3$ indicates no mass loss between 300 and 670 K, which confirms that the as-prepared perovskite is thermally stable up to 670 K as shown in Fig. 1(d). The decomposition of $CsSnCl_3$ takes place in two steps with a final temperature of about 820 K.

3.2. Optical properties

The study of the optical properties of perovskite materials in photovoltaic (PV) technologies plays a big part in understanding the optoelectronic nature of these technologies. In fact, UV-Vis spectroscopy is an accurate and convenient method to learn about the absorption behavior, get the various optical parameters, and clarify the band structure of semiconductor materials.[29] With the help of optical absorption studies, these characteristics can simply be identified by examining the interaction between the incident photons and the treated compounds.

The optical absorption of the $CsSnCl_3$ perovskite was determined by means of a UV-Vis spectrophotometer in the 250–800 nm wavelength range. Fig. 2(a) illustrates the absorption spectrum of the compound. The optical bandgap is a major factor in such fields of science as photovoltaics, solar cells, lasers, photoluminescence, and diodes.[30,31] Finding out whether the optical bandgap nature is direct or not represents, nonetheless, one of the most prominent features of perovskite materials.[32]

Overall, the character of the bandgap transition in semiconductor materials is experimentally identified by examining the absorption spectrum and calculating the optical absorption coefficient (α) of the compound. α could be found out from the absorption measurements bearing in mind that (e) refers to the cell thickness through the Beer–Lambert law:[33]

$$\alpha = \frac{2.303 \times A}{e} \quad (1)$$

α is generally related to the photon energy ($h\nu$) using the Tauc relation which is shown by the following equation.[34,35]

$$\alpha = \frac{\beta}{h\nu}\left(h\nu - E_g\right)^n \quad (2)$$

where β is a constant illustrating the degree of disorder, E_g refers to the optical bandgap, and n represents the power factor which shows the transition mode. It tends towards two values 1/2 or 2, which hinges upon whether the bandgap transition is direct or indirect and whether the transition is allowed or prohibited. The absorption and the emission of photons take place *via* allowed transitions for direct bandgap semiconductors (n = 1/2) while, for indirect bandgap semiconductors, the absorption

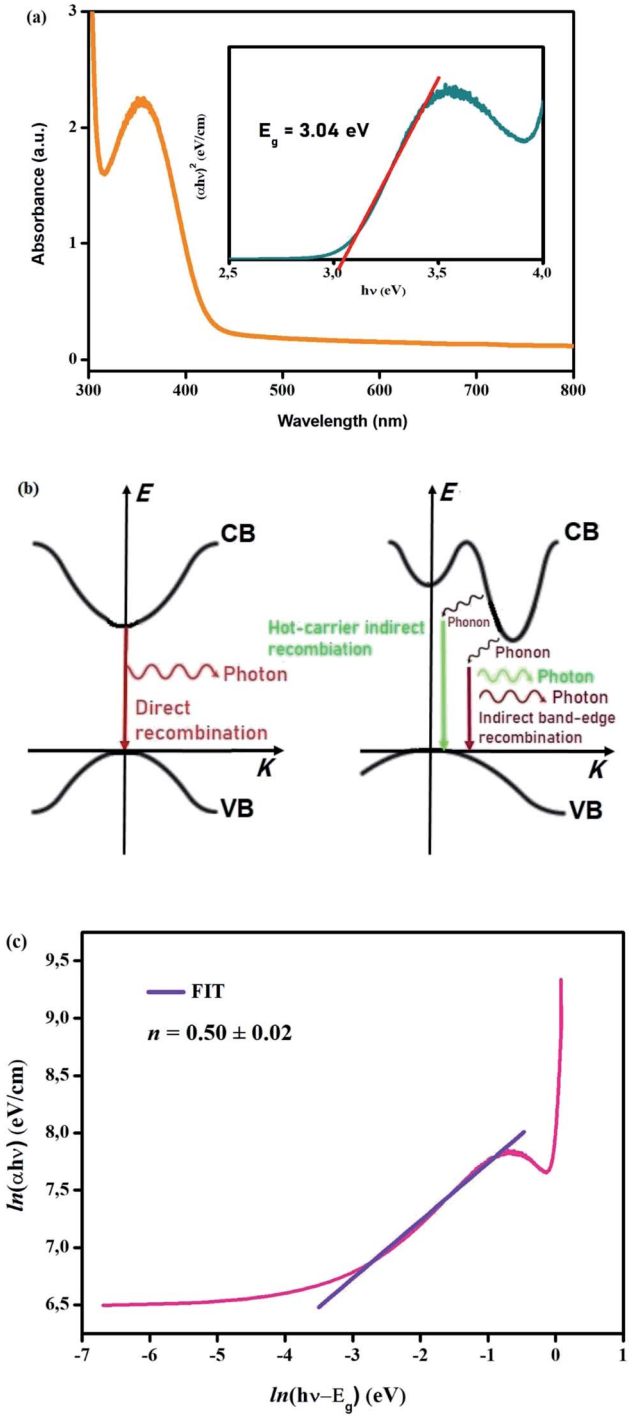

Fig. 2 (a) Absorbance spectrum of $CsSnCl_3$. The inset presents the Tauc plot for $CsSnCl_3$. (b) Direct and indirect band gaps. (c) Plot of $\ln(\alpha h\nu)$ *vs.* $\ln(h\nu'' - Eg)$.

and the recombination produce photons as well as phonons (Fig. 2(b)).

The calculation of the optical bandgap E_g is on the basis of the following Tauc formula:

$$(\alpha h\nu)^{1/n} = \beta(h\nu - E_g) \quad (3)$$

After plotting $(\alpha h\nu)^2$ and $(\alpha h\nu)^{1/2}$ as a function of the photon energy $(h\nu)$, the most appropriate and satisfactory plot is obtained when $n = 1/2$. The direct transition is chosen in accordance with the Tauc equation. Consequently,

$$(\alpha h\nu)^2 = \beta(h\nu - E_g) \quad (4)$$

As illustrated in the inset of Fig. 2(a), the bandgap E_g value could be calculated by means of the extrapolation of the linear portion to $\alpha = 0$.[36] E_g is found to be equivalent to 3.04 eV, proving that $CsSnCl_3$ is a potential candidate for optoelectronics.

In order to check the transition mode of the optical strip for our compound, the following equation is used to express:[37]

$$\ln(\alpha h\nu) = \ln(\beta) + n\ln(h\nu - E_g) \quad (5)$$

Accordingly, Fig. 2(c) displays the plot of the variation $\ln(\alpha h\nu)$ as a function of $\ln(h\nu - E_g)$. This curve provides a straight line where the slope is the power factor (n) which recognizes the type of optical transition mode.[37] In accordance with both Fig. 2(c) and eqn (5), the following linear relation is obtained:

$$\ln(\alpha h\nu) = 8.28 + 0.5\ln(h\nu - 3.04);\ (n \approx 1/2) \quad (6)$$

Therefore, the direct optical band transition mode of our material is verified. The determined value of the transition power factor (n) is almost equivalent to 1/2, which is in accord with the estimated mode.

3.3. Impedance spectroscopy results

Complex impedance spectroscopy (CIS) is a principal and successful procedure used in order to study the electrical behavior of a material. It provides information on the movement of ions within $CsSnCl_3$, the relaxation time, and the electrical conductivity.

The complex frequency-dependent impedance represents a non-destructive technique that demonstrates the bulk (grain), the grain boundary, and the electrode contribution in the material when applying the time-reversed electric field.[38] When an alternating field is forced, the charge carrier generally tends to become active and causes dipole orientation, charge displacement, and space charge formation. Hence, the contribution of grains, grain boundaries, and electrodes to the charge transport within the compound can be distinguished using the complex impedance study. The frequency-dependent impedance can be illustrated through eqn (7):

$$Z(\omega) = Z'(\omega) + jZ''(\omega) \quad (7)$$

Fig. 3(a) indicates the frequency variation in the real part (Z') of the complex impedance with various temperatures. In both phases, It is noticed that Z' decreases when frequency and temperature go up, which shows the negative temperature coefficient of the resistance (NTCR)-type behavior within the compound.[39,40] This type of behavior propounds that an increase in AC conductivity is possible owing to the rise in the mobility of charge carriers and also to the reduction in the

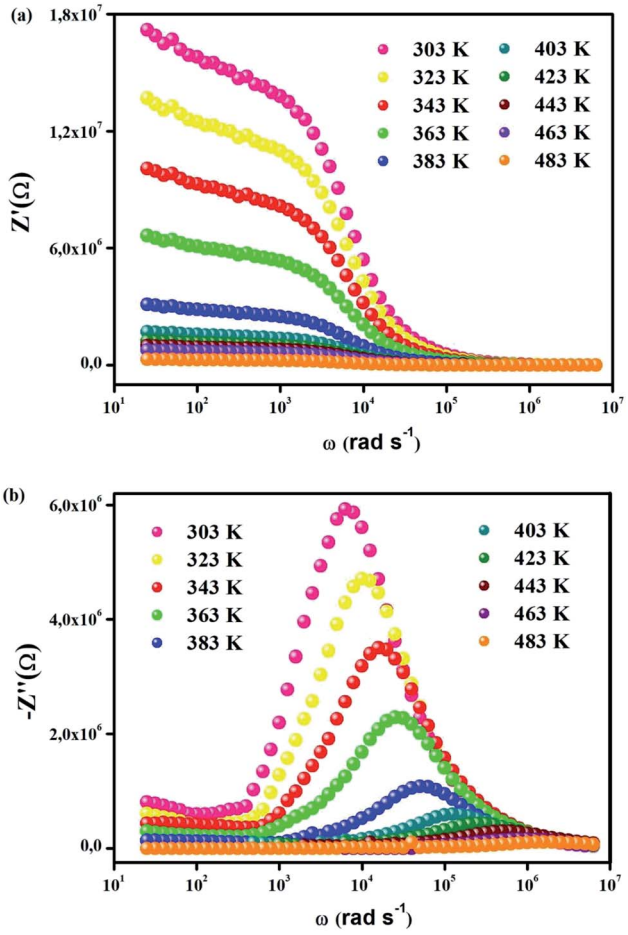

Fig. 3 (a) Real part of impedance (Z') *vs.* frequency, (b) imaginary part of impedance (Z'') *vs.* frequency.

trapped charge density in $CsSnCl_3$. Z' is temperature-independent in the high-frequency region, which points to the existence of space charge in the material. Space charge has less time to relax as soon as frequency augments. Hence, the fact that space charge polarization drops leads to a merging of curves at high frequency.[41] Fig. 3(b) displays the loss factor variation (Z'') in the whole frequency range of various temperatures. In both regions (monoclinic and cubic systems), this variation shows the basic charge transport mechanism and the relaxation process in $CsSnCl_3$ as a function of temperature. The immobile species/electrons at low temperatures and defects/vacancies at high temperatures seem to be the reasons behind the relaxation process. For each spectrum, a well-defined characteristic peak which was traditionally known as the "relaxation frequency" is noticed. The broadness peak shows a sharp deviation from an ideal Debye nature. The motion of charge carriers over a long-range which is essentially the cause of the transportation below the loss peak frequency contributes to the motion of the localized carriers above the relaxation frequency. With the rise of the temperature, the movement of the relaxation peak towards the high-frequency regime points to the thermally-dependent relaxation mechanism. Additionally, the peak height is reduced with temperature, suggesting the

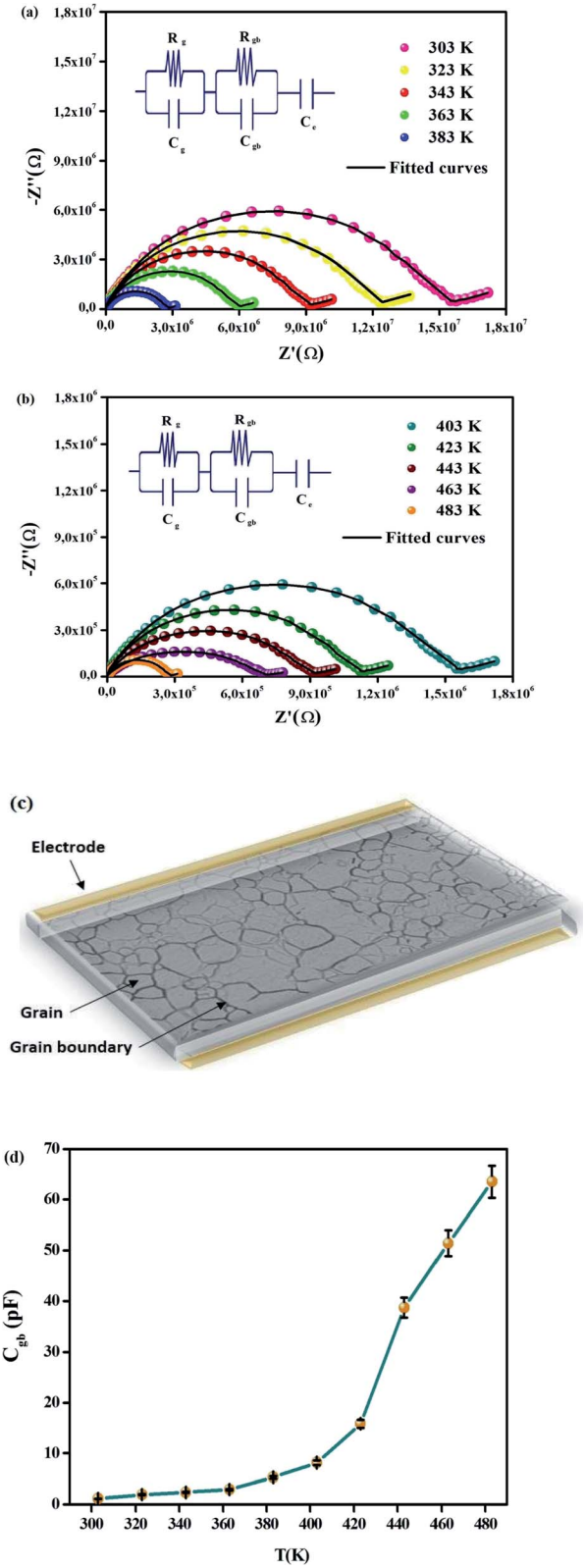

Fig. 4 (a), (b) Cole–Cole plot of $CsSnCl_3$ at different temperatures (equivalent circuit is shown in inset). (c) Schematic representation of grain and grain boundary within material. (d) Temperature dependence of grain boundary capacitance. The error bars are associated with the experimental accuracy (±4%).

Table 1 Equivalent circuit elements for the $CsSnCl_3$ compound at several temperatures

T (K)	R_g (kΩ)	C_g (nF)	R_{gb} (kΩ)	C_{gb} (pF)	C_e (μF)	α_e
303	101.21	1.78	1268.69	1.13	0.0642	0.4763
323	84.55	2.32	9445.87	1.96	0.0809	0.4712
343	61.88	2.87	765.48	2.42	0.0117	0.4521
363	40.18	3.14	498.23	2.96	0.212	0.4637
383	23.61	3.96	304.21	5.35	0.468	0.4895
403	9.35	4.42	171.56	8.16	0.852	0.4535
423	7.57	5.35	93.42	15.82	1.078	0.4637
443	5.54	6.63	63.98	38.75	1.747	0.4856
463	3.70	7.05	47.85	51.42	2.311	0.4825
483	1.93	7.89	23.67	63.52	2.759	0.4909

decrease in the grain and grain boundary resistance with temperature.[42]

The Cole–Cole plot in the temperature range of 303–483 K is illustrated in Fig. 4(a) and (b). It is worth mentioning that for both phases, the depressed semicircles have their centers below the real axis. This shows the non-Debye type of behavior in $CsSnCl_3$.[42] The decrease in the radii of the semicircles with the elevation of temperature in the Cole–Cole plot points once again to the NTCR behavior of the material.[43] Besides, this proves that the conduction process is thermally activated and that the compound possesses semiconducting proprieties. Three distinct semicircles which are most importantly in view of the contribution of electrode–material interface, grains, and grain boundaries ideally emerge in the Nyquist diagram. The semicircle in the high-frequency region indicates the contribution of the grain, whereas the semicircle in the low-frequency region denotes the contribution of grain boundaries. The semicircle in the ultra-low-frequency area shows the contribution owing to the electrode–material interface. Differentiating the involvement of grains and grain boundaries from the single depressed semicircle is deeply ambiguous. Consequently, the Maxwell–Wagner equivalent circuit model comprised of a parallel combination of a number of resistors (R) and capacitors (C) is used in order to distinguish the contribution of the grains and grain boundaries from the single semicircle. The impedance spectra of all temperatures are fitted with the help of the ZView Software. The desired circuit model is acquired in that case by linking two parallel RC elements in series, the straight line after the semicircle can be interpreted with the constant phase element (CPE) according to the double layer capacity of an inhomogeneous electrode surface (the inset of Fig. 4(a) and (b)). The diameter of the semicircle, *i.e.* the intersection point on the real axis, decreases significantly with the rise in temperature as illustrated in Fig. 4(a) and (b). This confirms the improvement in DC conductivity with higher temperatures.[44] A schematic representation of grains and grain boundaries in the material is illustrated in Fig. 4(c). The ZView software has been used to fit the experimental data in our paper in order to assess these parameters. It is noted that the value of R_{gb} is higher than the value of R_g for all temperatures as expressed in Table 1 which demonstrates that the grain boundaries have more contributions to the total resistance since $R = R_g + R_{gb}$. In fact, the grain boundaries in perovskite materials are more resistive than the grains. Because of polarization, the distinction between these two resistive values triggers a substantial growth in the number of space charges at the grain boundaries also known as the Maxwell–Wagner effect.[45]

The variation in grain boundary capacitance (C_{gb}) which is shown in Fig. 4(d) tends to go up with temperature. Grain

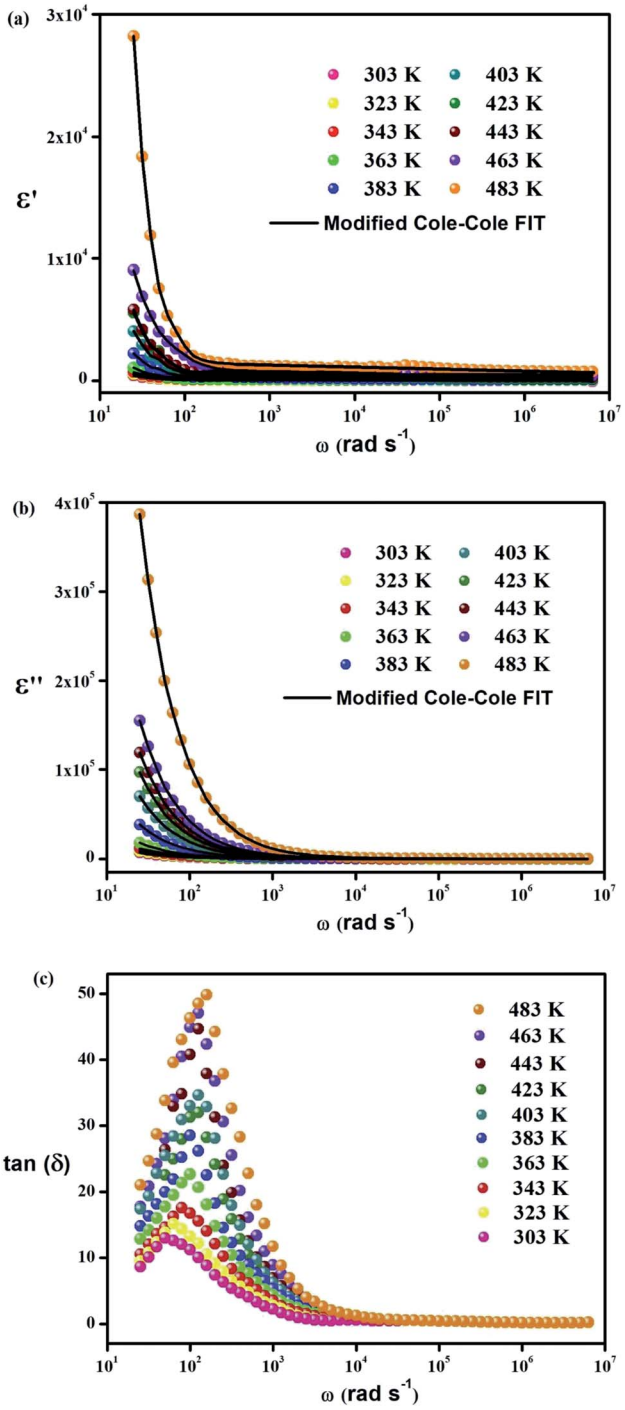

Fig. 5 (a) Frequency-dependent real part of dielectric permittivity. (b) Frequency-dependent imaginary part of dielectric permittivity. (c) tan δ *vs.* angular frequency spectra of $CsSnCl_3$.

boundary capacitance could be expressed as follows: $C_{gb} = (\varepsilon_{gb}A)/d$, where ε_{gb} refers to the intrinsic dielectric constant at the grain boundary. Hence, C_{gb} depends on the barrier-layer width (d), which is proportional to the ratio of trapped charge carriers in free carrier density.[38] The layer width becomes fairly small at high temperatures since trapped charge carriers drop as soon as the temperature rises. In fact, because of this behavior, grain boundary capacitance grows with temperature.

3.4. Dielectric properties

The dielectric response of any material could be illustrated through the following complex dielectric constant:

$$\varepsilon(\omega) = \varepsilon'(\omega) + j\varepsilon''(\omega) \quad (8)$$

where $\varepsilon'(\omega)$ which is the real part of the complex dielectric constant denotes the stored energy while $\varepsilon''(\omega)$ refers to the imaginary part of the dielectric constant and the energy dissipation of the applied electric field. Both the real and imaginary parts of the dielectric constant are expressed in eqn (9) and (10):

$$\varepsilon'(\omega) = \frac{Z''}{\omega C_0\left(Z'^2 + Z''^2\right)} \quad (9)$$

$$\varepsilon''(\omega) = \frac{Z'}{\omega C_0\left(Z'^2 + Z''^2\right)} \quad (10)$$

where $C_0 = (\varepsilon_0 A)/d$ (C_0 represents the free space capacitance, ε_0 indicates the permittivity of free space, A refers to the area of the electrode and d shows the pellet thickness).

The difference between the dielectric constants is investigated as a function of frequency in the temperature range of 303–483 K. For both phases, Fig. 5(a) and (b) confirm that, in the low-frequency region, the dielectric constant is wide at a certain temperature and slowly goes down with the rise in frequency. Both $\varepsilon'(\omega)$ and $\varepsilon''(\omega)$ play a big part in the ionic conduction process which is controlled by four main types of polarization, *viz.* ionic, electronic, orientational, and interfacial.

Ionic and electronic polarizations refer to the deformational component of polarizability, whereas orientational and interfacial polarizations represent the relaxation component of polarizability.[46] The variation in the real part of permittivity with frequency could be interpreted *via* Maxwell–Wagner interfacial polarization, which is in accord with Koop's phenomenological theory.[47]

The material in this model is expected to include conducting grains that are separated by poorly conducting grain boundaries. Therefore, to restrain their flow, charge carriers get trapped at the interface of grain boundaries.[47,48] The exchange of electrons between the ions belonging to the same molecules occurs in the interfacial polarization process. The deformities and imperfections found in the material are the reason for changing the position and the distribution of positive and negative space charges. Influenced by the applied electric field, positive and negative charges shift towards the negative and positive poles of the applied field respectively.[49]

We note that for the two phases (monoclinic and cubic system), electrons can reach the grain boundary regime through hopping (Fig. 5(a)) in the low-frequency region but they are accumulated at the grain boundary position and cause polarization due to the high grain boundary resistance. On the other hand, electrons cannot follow the alternation of the applied field at high frequency, which avoids further accumulation of electrons even if they move in the reverse direction. Consequently, the possibility of arriving at the grain boundary diminishes for electrons when frequency increases which thin polarization.[49] At the mid-frequency region, the variation in $\varepsilon'(\omega)$ can be typified by the appearance of a hump on account of the relaxation process. The movement of the hump position with temperature to the low-frequency region puts forth a temperature-dependent dielectric response. However, at high frequency, the value of $\varepsilon'(\omega)$ does not change considerably. This "unrelaxed" value of permittivity shows the atomic and electronic polarization. The $CsSnCl_3$ perovskite crystal includes Cs^+, Sn^{2+}, and Cl^- ions which play a big part in its polarization. Therefore, the real part of the dielectric constant $\varepsilon'(\omega)$ goes down with the decline in temperature, which is probably because of the low responsive nature of the participating ions and the conducting electrons at low temperature.

Among various popular theoretical models, the modified Cole–Cole model has been used with DC conductivity to

Table 2 Estimated values of the parameters β. m. σ_{sp}. and σ_{fc}. τ obtained from the fitting of the modified Cole–Cole model and the parameters a and b found by the fitting of $M''(\omega)$ with the modified KWW function

	Parameter							
T (K)	f_{max}	τ	β	m	σ_{sp}	σ_{fc}	a	b
303	1.45×10^4	6.89×10^{-5}	0.659	0.789	3.57×10^{-5}	8.56×10^{-4}	0.578	0.503
323	2.76×10^4	3.62×10^{-5}	0.785	0.806	8.91×10^{-5}	9.89×10^{-4}	0.598	0.552
343	4.95×10^4	2.02×10^{-5}	0.795	0.813	2.68×10^{-4}	1.65×10^{-3}	0.612	0.621
363	7.68×10^4	1.30×10^{-5}	0.801	0.825	6.35×10^{-4}	4.48×10^{-3}	0.633	0.675
383	1.35×10^5	7.36×10^{-6}	0.875	0.847	9.15×10^{-4}	7.31×10^{-3}	0.678	0.699
403	4.13×10^5	2.41×10^{-6}	0.657	0.869	4.88×10^{-3}	1.45×10^{-2}	0.745	0.728
423	5.02×10^5	1.99×10^{-6}	0.854	0.911	9.09×10^{-3}	3.68×10^{-2}	0.789	0.743
443	6.28×10^5	1.59×10^{-6}	0.932	0.936	3.72×10^{-2}	5.51×10^{-2}	0.825	0.762
463	7.83×10^5	1.27×10^{-6}	0.912	0.942	5.03×10^{-2}	7.08×10^{-2}	0.869	0.789
483	8.78×10^5	1.13×10^{-6}	0.928	0.966	8.68×10^{-2}	9.74×10^{-2}	0.881	0.825

examine the variation in the dielectric constant and the dielectric loss as a function of frequency for different temperatures.[50] Per the modified Cole–Cole model, the complex permittivity is shown as follows:

$$\varepsilon^* = \varepsilon_\infty + \frac{\varepsilon_s - \varepsilon_\infty}{1 + (j\omega\tau)} - \frac{j\sigma^*}{\varepsilon_0\omega^m} \quad (11)$$

$$\varepsilon' = \varepsilon_\infty + \left[\frac{(\varepsilon_s - \varepsilon_\infty)\left\{1 + (\omega\tau)^\beta \cos\left(\frac{\beta\pi}{2}\right)\right\}}{1 + 2(\omega\tau)^\beta \cos\left(\frac{\beta\pi}{2}\right)}\right] + \frac{j\sigma}{\varepsilon_0\omega^m} \quad (12)$$

where σ* is the summation of space charge carrier conductivity (σ_{sp}) and free charge carrier conductivity (σ_{fc}), ε_s represents the low-frequency limit of permittivity and ε_∞ indicates the high-frequency limit of permittivity. M refers to the frequency exponent while β stands for the modified Cole–Cole parameter which has a value between 0 and 1. τ is the relaxation time. The real (ε') and imaginary (ε'') parts of the dielectric constant are illustrated in eqn (13) and (14):

$$\varepsilon' = \varepsilon_\infty + \left[\frac{(\varepsilon_s - \varepsilon_\infty)\left\{1 + (\omega\tau)^\beta \cos\left(\frac{\beta\pi}{2}\right)\right\}}{1 + 2(\omega\tau)^\beta \cos\left(\frac{\beta\pi}{2}\right) + (\omega\tau)^\beta}\right] + \frac{\sigma_{sp}}{\varepsilon_0\omega^m} \quad (13)$$

$$\varepsilon'' = \left[\frac{(\varepsilon_s - \varepsilon_\infty)(\omega\tau)^\beta \sin\left(\frac{\beta\pi}{2}\right)}{1 + 2(\omega\tau)^\beta \cos\left(\frac{\beta\pi}{2}\right) + (\omega\tau)^\beta}\right] + \frac{\sigma_{fc}}{\varepsilon_0\omega^m} \quad (14)$$

The experimental data of ε' and ε'' are fitted with the modified Cole–Cole equation. The obtained values of such various parameters as β, m, σ_{sp}, σ_{fc}, and τ are mentioned in Table 2. According to Table 2, it is obvious that the values of space charge conductivity (σ_{sp}) and free charge conductivity (σ_{fc}) go up as soon as the temperature rises. The value of β which is between 0 and 1 further proves the non-Debye nature. The relaxation time declines the moment the temperature climbs.

The loss tangent represents the ratio of the dielectric loss and the real part of the dielectric constant. Fig. 5(c) illustrates the variation in the loss tangent with frequency for a particular range of temperature ($\tan(\delta) = \varepsilon'(\omega)/\varepsilon''(\omega)$). For the two regions, the loss tangent decreases when the frequency rises and then becomes constant in the high-frequency region at a given temperature. The appearance of the peaks in the low-frequency region may be caused by the dominant dipolar polarization. Loss tangent values increase and peaks thus move as soon as the temperature climbs, which proves that dipolar polarization is a thermally controlled mechanism. The loss peak ultimately emerges the moment the hopping frequency corresponds obviously to the frequency of an applied external AC field. In addition, the hopping mechanism propounds that the electrical conductivity is elevated with temperature which brings about the thermally activated charge carriers.

3.5. Modulus analysis

The detailed complex modulus spectra have been examined to study the relaxation procedure in $CsSnCl_3$. The complex electric

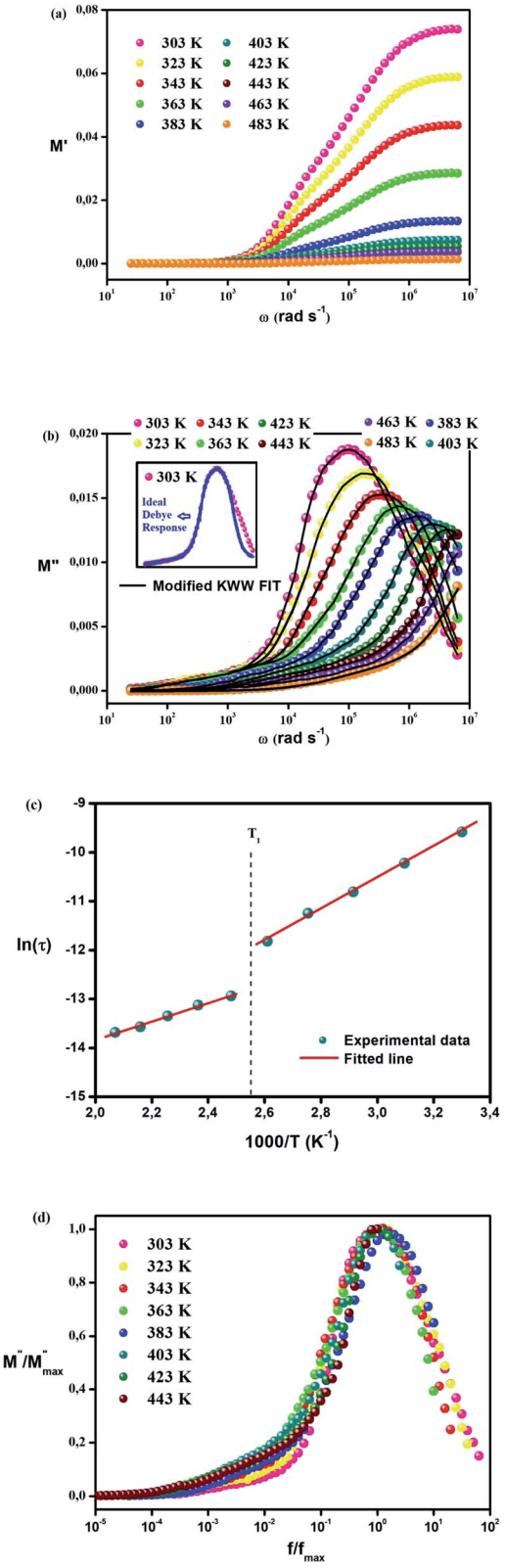

Fig. 6 (a) Frequency dependence of the real part of electric modulus of $CsSnCl_3$. (b) Frequency dependence of the imaginary part of the electric modulus of the sample. Inset of (b) deviation from the ideal Debye response at 303 K. (c) Arrhenius plot of the maximum frequency of M'' (ω) of the sample. (d) Normalized imaginary electric modulus M''/M''_{max} *vs.* f/fmax at different temperatures.

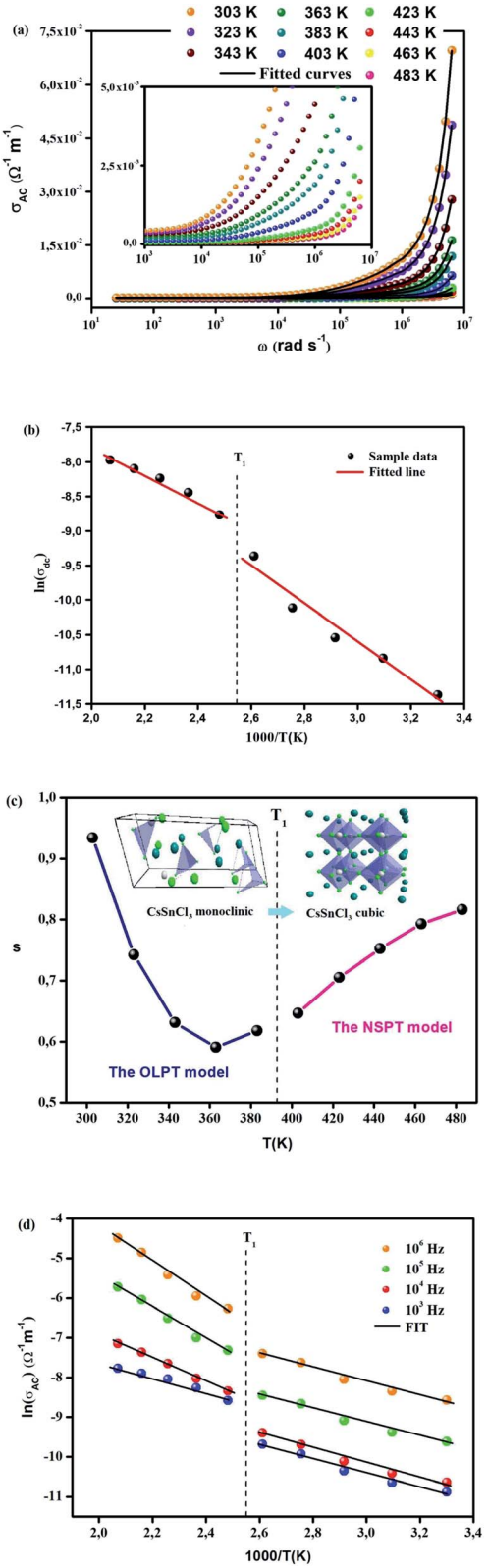

Fig. 7 (a) Variation in AC conductivity of $CsSnCl_3$ with frequency at different temperatures. (b) σ_{DC} *vs.* 1000/T plot of $CsSnCl_3$. (c) Temperature dependence of s for $CsSnCl_3$. (d) Temperature dependence of the ln(σ_{AC}) at different frequencies.

modulus which is essentially the reciprocal of complex permittivity suggested by Macedo is an incredibly simple tool to research the electrical relaxation mechanism of space charge distribution by stopping the effect of electrodes. The electric modulus mainly shows the electric field relaxation in the material as soon as the dielectric displacement is continuous. The electric modulus is expressed through the following equation:

$$M^* = \frac{1}{\varepsilon^*} = \frac{1}{(\varepsilon' + j\varepsilon'')} = \frac{\varepsilon'}{\varepsilon'^2 + \varepsilon''^2} + i\frac{\varepsilon'}{\varepsilon'^2 + \varepsilon''^2} = M' + iM'' \quad (15)$$

where M', M'', ε' and ε'' represent the real and imaginary parts of the electric modulus (M^*) and the dielectric constant (ε^*) respectively.[51–55]

Fig. 6(a) describes the real part of the electric modulus spectra as a function of frequency for different temperatures. The variation in M' with frequency illustrates that M' obtains an extremely small value (almost zero) in the low-frequency region for all temperatures. This behavior along with the sigmoidal nature of M' is caused by the long-range mobility of charge carriers in the conduction mechanism and the negligence of the electrode polarization. There is a minor change in the peak of M' with the increase in temperature along the high-frequency region.

Fig. 6(b) illustrates the variation in the imaginary part of the electric modulus M'' with frequency at various temperatures. For both phases, M'' obtains its maximum value at a particular temperature, causing a peak at a certain frequency which amounts to the relaxation frequency. In the low-frequency region, no peak occurs while there is a significant peak that is noticed in the high-frequency region. In the low-frequency region, charge carriers can move easily over a long distance showing the successful charge carrier hopping from one site to another. However, charge carriers are restricted in their potential well and make a controlled motion in the high-frequency region. As a result, the peak occurrence provides information concerning the transition from long-range to short-range mobility of charge carriers. The peaks in M'' tend to move to the high-frequency region with a rise in temperature, which can be set out by the hopping mechanism. The non-Debye response of the sample is demonstrated by the asymmetrical nature of the peaks in M''. To interpret the asymmetric nature of peaks in the imaginary part of the electric modulus, a KWW equation is used as follows (16):[51–55]

$$M''(\omega) = \frac{M''_{max}}{\frac{(1-c)}{(a+b)}\left[b\left(\frac{f}{f_{max}}\right)^{-a} + a\left(\frac{f}{f_{max}}\right)^{b}\right] + c} \quad (16)$$

where M''_{max} denotes the maximum value of the imaginary part of the electric modulus and the corresponding frequency is referred to as f_{max}, a and b represent two independent shape parameters for low and high-frequency sides respectively and c is the smoothing parameter. Eqn (16) is reduced to eqn (19) if $a = b = 1$ and $c = 0$, which indicates the ideal Debye type of behavior providing the symmetrical nature of M'' spectra as a function of frequency. The fitting of the modified KWW

function is confirmed by the solid line as shown in Fig. 6(b), whereas Table 2 sums up the values of various parameters. The values of a and b proliferate with the increase in temperature, suggesting that $M''(\omega)$ becomes close to the ideal Debye-type response when the temperature goes up. For $CsSnCl_3$, the deviation of the ideal Debye response occurring at 303 K in the low and high-frequency sides of the experimental data is illustrated in the inset of Fig. 6(b);

$$M''(\omega) = \frac{M''_{\max}}{\frac{1}{2}\left[\left(\frac{f_{\max}}{f}\right) + \left(\frac{f}{f_{\max}}\right)\right]} \quad (17)$$

The relaxation time is estimated *via* eqn (18);

$$\tau = \frac{1}{f_{\max}} \quad (18)$$

The average activation energy of the charge carriers could be calculated based on the Arrhenius equation as stated in eqn (19);

$$\tau = \tau_0 \exp\left(-\frac{E_a}{k_\beta T}\right) \quad (19)$$

The phase transition appearing in DSC diagrams from the monoclinic to the cubic system is confirmed by the change of the curve slope at $T = 391/393$ K (Fig. 6(c)). 0.27 and 0.16 eV represent the derived activation energy from the slope of the least square fitting of ln τ *vs.* $1000/T$ plot for the phase 1 ($CsSnCl_3$ monoclinic) and 2 ($CsSnCl_3$ cubic), successfully. Additionally, this demonstrates that, in $CsSnCl_3$, the conduction mechanism is on account of the thermally-stimulated charge carriers.[56]

Fig. 6(d) displays the variation in the normalized imaginary part of the electric modulus with the normalized frequency of the examined sample for various temperatures. The peak positions of the normalized spectrum show the transition from long-range mobility to short-range mobility of charge carriers as well as the hopping method of charge carriers as previously explained in detail in the case of M'' spectra.[57] The coincidence of the peaks at all temperatures emphasizes the temperature-independent performance of dynamic processes occurring in the sample.

3.6. AC electrical conductivity

Fig. 7(a) exhibits the variation in temperature-dependent AC conductivity as a function of frequency. The AC electrical conductivity is estimated using of the following relation $\sigma_{ac} = \omega\varepsilon'\varepsilon_0 \tan\delta$ where ε_0 denotes the permittivity of free space. In our work, the estimated conductivity in the low-frequency region is ascribed to DC conductivity, whereas conductivity in the high-frequency region is caused by AC conductivity. Due to the contribution of frequency-independent and temperature-dependent DC conductivity, the curves tend to be flattened in the low-frequency region.[54] Nevertheless, the curves of the electrical conductivity become a lot larger and point to a strong frequency dispersion with the rise in frequency, which is on account of the contribution of AC conductivity. In this type of variation, the frequency at which the transition of conductivity occurs is known as "frequency hopping" (ω_P). The latter tends to move to the high-frequency region when the temperature climbs. The spotted frequency-independent DC conductivity and frequency-dependent AC conductivity can be illuminated by the theory of the jump relaxation model (JRM) propounded by Funke.[58] Per this theory, the ions in the low-frequency region can hop successfully to their neighboring sites. Long-term availability supports these successful jumps which result in a long-range translational motion of ions devoted to DC conductivity but both successful and unsuccessful hopping occur in the high-frequency region.

The hopping ion can jump back to its initial site (forward–backward–forward motion) causing an unsuccessful hopping. However, in successful hopping, the excited jumping ion hops to a new site and becomes steady in the new position while the neighboring ions become relaxed with this stationary ion. The ratio of successful and unsuccessful hopping increases in the high-frequency region leading to dispersive conductivity there. The measured electrical conductivity is attributed to Jonscher's power law-*i.e.* the universal dielectric response (UDR) model which was suggested by Jonscher;[59]

Table 3 Parameters determined from the OLPT and NSPT models at several frequencies

		Frequency (Hz)			
		10^3	10^4	10^5	10^6
The OLPT model	α (Å^{-1})	0.59	0.63	0.69	0.74
	W_{H0} (eV)	0.48	0.43	0.42	0.41
	N (cm^{-3})	7.98×10^{26}	1.14×10^{27}	2.68×10^{27}	3.85×10^{27}
	r_p (Å)	1.12	1.08	1.01	0.98
	R_ω (Å)	4.10	3.98	3.95	3.87
	ε_p (F m^{-1})	1.11×10^{-9}	2.80×10^{-9}	3.69×10^{-9}	5.75×10^{-9}
	W_H (eV)	0.32	0.30	0.28	0.27
The NSPT model	α (Å^{-1})	0.76	0.81	0.86	0.92
	$N(E_F)$ (eV^{-1} cm^{-3})	6.68×10^{29}	8.74×10^{29}	2.68×10^{30}	4.01×10^{30}
	R_ω (Å)	3.61	3.59	3.56	3.48

$$\sigma_{AC}(\omega) = \sigma_{DC} + \sigma_0 f^s \quad (20)$$

where σ_{AC} and σ_{DC} denote the AC and DC contribution of total conductivity, respectively, σ_0 refers to a constant and s depicts the frequency exponent. The value of s which essentially represents the interaction of charge carriers with the lattice of the sample is between 0 and 1. The UDR model is used to match the experimental data of the frequency-dependent conductivity of the sample (Fig. 7(a)).

However, σ_{DC} values are calculated at various temperatures by non-linear curve fitting of σ_{AC} using the UDR model. The activation energy (E_a) of $CsSnCl_3$ are further estimated based on the ln σ_{DC} *vs.* $1000/T$ plot (Fig. 7(b)) *via* the Arrhenius equation:

$$\sigma_{DC} = \sigma_0 e^{\frac{-E_a}{k_B T}} \quad (21)$$

where σ_0 refers to the pre-exponential factor, E_a represents the activation energy, k indicates the Boltzmann constant and T stands for the absolute temperature.

The phase transition is confirmed by the change of the slope of a curve at $T = 391/393$ K. The energy activation values of $CsSnCl_3$ were found to be 0.23 (phase 1) and 0.16 eV (phase 2), which are so close to the values obtained from the M'' spectra.

A convenient pattern based on the various theoretical models associating it with $s(T)$ behavior may be proposed to establish the conduction mechanism in the $CsSnCl_3$ compound.[60] Several patterns which are in agreement with the literature are suggested based on two distinctive procedures, typical barrier hopping, and quantum mechanical tunneling, or a mixture of the two. Besides, it is thought that atoms or electrons (or polarons) are carriers in various ways. The diverse models are the quantum mechanical tunneling (QMT), the correlated barrier hopping (CBH), the non-overlapping small-polaron tunneling (NSPT) and also the overlapping large polaron tunneling (OLPT).[61–63]

Fig. 7(c) presents the temperature dependence of the exponent s which confirms the phase transition appearing in DSC diagrams at $T = 391/393$ K from the monoclinic to the cubic system:

−Phase 1 ($CsSnCl_3$ cubic): the exponent s reaches a minimum value when the temperature rises and then increases slightly. Accordingly, the (OLPT) model is well-chosen.

−Phase 2 ($CsSnCl_3$ monoclinic): the exponent s increases with the temperature, which demonstrates that the (NSPT) model is the suitable one.

In fact, within $CsSnCl_3$, negatively charged chloride ions exist in the environment of Cs^+ and Sn^{2+} ions but the two charge centers do not coincide, which results in a partially polar material. The polaron is formed as soon as the localized charge comes close to the compound and moves to the nearest neighboring positions. After the movement of the polaron to a new configuration, it either is stable at that position ("successful hop") or shifts towards the reverse direction so as to get a partially relaxed configuration also known as "unsuccessful hop". At low frequency, the non-dispersive behavior of the AC conductivity emerges owing to the successful hopping of the polaron. However, with the increase in frequency, some hops become unsuccessful. Accordingly, conductivity becomes dispersive at a high frequency. In the majority of the inorganic halide perovskite materials, a polaron is believed to be caused by lattice distortion[64] which is ignored in the quantum mechanical tunneling of electrons. When the polarons are formed because of adding a charge carrier to a site, they can trigger a high degree of local lattice distortion. These polarons are so confined that their cloud distortions do not overlap. The AC conductivity at high temperatures is explained by the tunneling of carriers or polarons trapped at structural defects.

The AC conductivity in the OLPT model is ensured by the polaron tunneling mechanism. An overlap of the polaron distortion clouds comes off. The spatial extent of the polaron is wider than the interatomic spacing in the case of large polarons for which the overlap of the potential wells at the neighboring sites can occur because of the long-range character of the Coulomb interaction. Consequently, the polaron hopping energy diminishes, making an impact on the loss as a function of frequency since the activation energy related to the motion of the charge carriers between the various sites decreases as shown through:[62]

$$W_H = W_{H0} \times \left(1 - \frac{r_p}{R}\right) \quad (22)$$

where r_P represents the radius of the large polaron and W_H refers to the polaron hopping energy.

W_{H0} is expressed as follows:[60]

$$W_{H0} = \frac{e^2}{4\varepsilon_p r_p} \quad (23)$$

where ε_P is the effective dielectric constant. For the OLPT model, W_{H0} is expected to be a constant for all sites while the intersite separation (R) denotes a variable.

The AC conductivity is presented through the following equation:[60]

$$\sigma_{ac} = \frac{\pi^4 e^2 k_B^2 T^2 \alpha^{-1} \omega \, [N(E_F)]^2 R_\omega^4}{12\left(2\alpha k_B T + W_{H0} r_p / R_\omega^2\right)} \quad (24)$$

where the hopping length (R_ω) is estimated as follows:

$$(R'_\omega)^2 + (\beta W_{H0} + \ln(\omega\tau_0))R'_\omega - \beta W_{H0} r'_p = 0 \quad (25)$$

where $R'_\omega = 2\alpha R_\omega$, $\beta = 1/k_B T$, $r'_P = 2\alpha r_P$ and α represents the inverse localization length.

In the OLPT model, s corresponds to the following equation:[62]

$$s = 1 - \frac{8\alpha R_\omega + \frac{6\ W_{H0} r_p}{R_\omega k_B T}}{\left[2\alpha R_\omega + \frac{W_{H0} r_p}{R_\omega k_B T}\right]^2} \quad (26)$$

The theoretical calculations of the OLPT approach which is used in phase 1 (Fig. 7(d)) fit well with the experimental data (eqn (24)). Table 3 presents the values of α, W_{H0}, $N(E_F)$, r_P, and R_ω. W_H and ε_P values are calculated in eqn (22) and (23),

respectively as mentioned in Table 3. The obtained values of $N(E_F)$ are logical for localized states. α values are of the same order as discussed by Murawski *et al.*[62] Fig. 8(a) shows the variation of the tuning distance "R_ω" which decreases with frequency as a function of ln(f) (phase 1).

In the NSPT model, the exponent s could be calculated *via* the following equation:[65]

$$s = 1 + \frac{4k_B T}{W_m - k_B T \ln(\omega\tau_0)} \quad (27)$$

where the characteristic relaxation time τ_0 is supposed to be 10^{-13} s (the order of atom vibrational period) and W_m represents the activation energy for polaron transfer while K_B shows the Boltzmann constant and T refers to temperature.

For the great values of $W_m/k_B T$, s changes into:

$$s = 1 + \frac{4k_B T}{W_m} \quad (28)$$

The curve fitting (Fig. 8(b)) is employed to calculate the value of W_m, which is equivalent to 0.161 eV.

In the NSPT model, the activation energy for polaron transfer (W_m) does not depend on the intersite separation[65] since small polarons are confined in such a way that their cloud distortions do not overlap. For the NSPT model, the AC conductivity is expressed as follows.[63]

$$\sigma_{ac} = \frac{(\pi e)^2 k_B T \alpha^{-1} \omega [N(E_F)]^2 R_\omega^4}{12} \quad (29)$$

where

$$R_\omega = \frac{1}{2\alpha}\left[\ln\left(\frac{1}{\omega\tau_0}\right) - \frac{W_m}{k_B T}\right] \quad (30)$$

where R_ω represents the tunneling distance, α^{-1} denotes the spatial extension of the polaron and $N(E_F)$ refers to the density of states near the Fermi level.

Fig. 7(d) shows the temperature dependence of ln(σ_{AC}) at various frequencies. This figure indicates that the fit accords with the experimental data (phase 2). The dissimilar parameters calculated for the (NSPT) model are mentioned in Table 3.

The values of the density of states $N(E_F)$ are adequate for the localized states.[65] Fig. 8(c) illustrates the variation in the parameters α and $N(E_F)$ as a function of frequency. The increase in the two parameters α and $N(E_F)$ with the frequency is noticed, which is in agreement with the literature.[53]

Table 3 shows the values of R_ω interpreted based on eqn (30). Fig. 8(a) confirms the variation in R_ω as a function of frequency. It is obvious that the values of the tunneling distance for the two phases have the same range of the interatomic spacing Cs–Cl (3.55–4.14 Å).[27] Moreover, the value of the tunneling distance diminishes faster when frequency increases. This behavior proposes that the charge carriers shift from the long-distance toward the short-distance tunneling. This behavior can be the reason for the rise in $N(E_F)$ ($\sim 10^{30}$ eV^{-1} cm^{-3}) with the frequency.[60] The values of R_ω (3.48–4.10 Å) and the distances Cs–Cl (3.55–4.14 Å) are close, which implies that due to the mobility of Cs^+ in the compound, the AC conductivity is ensured by large or small polaron motion.

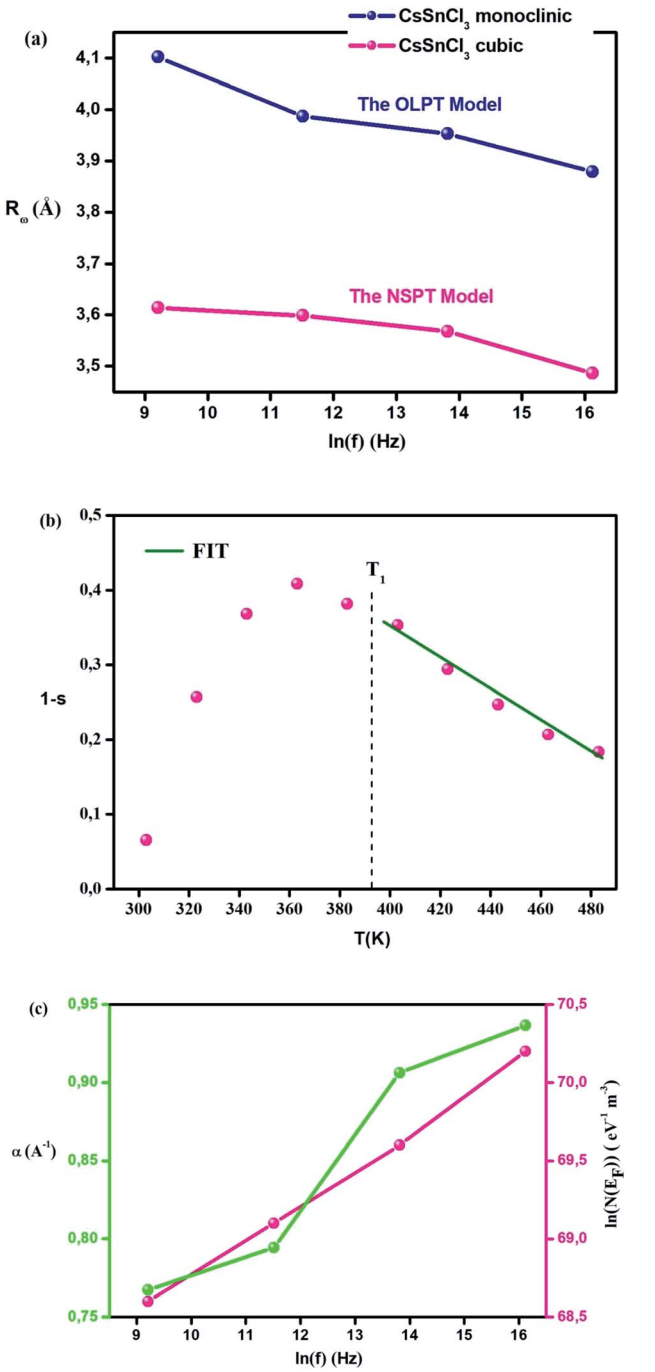

Fig. 8 (a) Variation of AC conductivity parameter $R\omega$ (Å) according to the frequency in the monoclinic and cubic system for $CsSnCl_3$. (b) Temperature dependence of 1 s for $CsSnCl_3$. (c) Variation in the parameters α(Å^{-1}), $N(E_F)$ (eV^{-1} cm^{-3}) *vs.* the frequency.

4. Conclusions

In summary, $CsSnCl_3$ has been synthesized using the slow evaporation solution growth technique. Phase transformation

(from monoclinic to cubic) has been assured by PXRD and DSC measurements and demonstrated by the study of the dielectric properties. The direct bandgap of this sample was 3.04 eV. A general investigation has been conducted on complex impedance, relative permittivity, complex modulus and AC conductivity for the 10^{-1}–10^{6} Hz frequency range with various temperatures. The frequency dependence of the AC conductivity which was explained by Jonscher's law has been researched as a function of temperature. The conduction mechanism which was interpreted by several models based on Elliott's theory might be assigned in phase 1 to tbibhe overlapping large polaron tunneling (OLPT) model and to the non-overlapping small polaron tunneling (NSPT) model in phase 2. The analysis of these various models (OLPT and NSPT) for which Elliott's variables were calculated suggested that the mobility of Cs^{+} ions ensured the alternative current conduction in $CsSnCl_3$ *via* the tunneling mechanism.

Conflicts of interest

There are no conflicts to declare.

Acknowledgements

We are grateful for the financial support provided by the Ministry of Higher Education and Scientific Research of Tunisia. We would also like to express our thanks to Sabriya Mbarek, an English Language Teacher at the Faculty of Science - Sfax, Tunisia for proofreading this paper.

References

1 Q. Jiang, L. Q. Zhang, H. L. Wang, X. L. Yang, J. H. Meng, H. Liu, Z. G. Yin, J. L. Wu, X. W. Zhang and J. B. You, *Nat. Energy*, 2017, **2**, 16177.
2 Q. Jiang, Y. Zhao, X. W. Zhang, X. L. Yang, Y. Chen, Z. M. Chu, Q. F. Ye, X. X. Li, Z. Z. Yin and J. B. You, *Nat. Photonics*, 2019, **13**, 460.
3 W. Zhang, G. E. Eperon and H. J. Snaith, *Nat. Energy*, 2016, **1**, 1.
4 P. Sadhukhan, S. Kundu, A. Roy, A. Ray, P. Maji, H. Dutta, S. K. Pradhan and S. Das, *Cryst. Growth Des.*, 2018, **18**, 3428.
5 S. Ananthakumar, J. R. Kumar and S. M. Babu, *J. Photonics Energy*, 2016, **6**, 42001.
6 P. Maji, A. Ray, P. Sadhukhan, A. Roy and S. Das, *Mater. Lett.*, 2018, **227**, 268.
7 A. Babayigit, *et al.*, *Sci. Rep.*, 2016, **6**, 18721.
8 G. E. Eperon, *et al.*, *ACS Nano*, 2015, **9**, 9380.
9 A. Babayigit, *et al.*, *Nat. Mater.*, 2016, **15**, 247.
10 M. Roknuzzaman, K. Ostrikov, *et al.*, *Sci. Rep.*, 2017, **7**, 14025.
11 L. Peedikakkandy and P. Bhargava, *RSC Adv.*, 2016, **6**, 19857.
12 T. C. Jellicoe, *et al.*, *J. Am. Chem. Soc.*, 2016, **138**, 2941.
13 H. Ayatullahah, *et al.*, *Acta Phys. Polym.*, 2013, **124**, 102.
14 L. Huang and W. R. L. Lambrecht, *Phys. Rev. B*, 2013, **88**, 165203.
15 X. Mao, L. Sun, T. Wu, T. Chu, W. Deng and K. Han, *J. Phys. Chem. C*, 2018, **122**, 7670.
16 M. H. Kumar, S. Dharani, W. L. Leong, P. P. Boix, R. R. Prabhakar, T. Baikie, C. Shi, H. Ding, R. Ramesh, M. Asta, M. Graetzel, S. G. Mhaisalkar and N. Mathews, *Adv. Mater.*, 2014, **26**, 7122.
17 H. Xu, J. Duan, Y. Zhao, Z. Jiao, B. He and Q. Tang, *J. Power Sources*, 2018, **399**, 76.
18 D. Sabba, H. K. Mulmudi, R. R. Prabhakar, T. Krishnamoorthy, T. Baikie, P. P. Boix, S. Mhaisalkar and N. Mathews, *J. Phys. Chem. C*, 2015, **119**, 1763.
19 I. Chung, J.-H. Song, J. Im, J. Androulakis, C. D. Malliakas, H. Li, A. J. Freeman, J. T. Kenney and M. G. Kanatzidis, *J. Am. Chem. Soc.*, 2012, **134**, 8579.
20 F. Hao, C. C. Stoumpos, D. H. Cao, R. P. H. Chang and M. G. Kanatzidis, *Nat. Photonics*, 2014, **8**, 489.
21 J. Islam and A. K. M. Akther Hossain, *Sci. Rep.*, 2020, **10**, 14391.
22 P. Maji, A. Ray, P. Sadhukhan, S. Chatterjee and S. Das, *J. Appl. Phys.*, 2018, **124**, 124102.
23 S. Das and A. Ghosh, *J. Phys. Chem. B*, 2017, **121**, 5422.
24 C. Tealdi, G. Chiodelli, L. Malavasi, G. Flor, C. Fisica, I. C. N. R. Unita, V. Taramelli and I. Pavia, *J. Mater. Chem.*, 2004, **14**, 3553.
25 T. Paul and A. Ghosh, *J. Appl. Phys.*, 2017, **121**, 135106.
26 See http://mill2.chem.ucl.ac.uk/tutorial/lmgp/celref.htm.
27 F. R. Poulsen and S. E. Rasmussen, *Acta Chem. Scand.*, 1970, **24**, 150.
28 K. Yamada, Y. Kuranaga, K. Ueda, S. Goto, T. Okuda and Y. Furukawa, *Bull. Chem. Soc. Jpn.*, 1998, **71**, 127.
29 S. A. Khan, F. S. Al-Hazmi, S. Al-Heniti, A. S. Faidah and A. A. Al-Ghamdi, *Curr. Appl. Phys.*, 2010, **10**, 145.
30 J. Lv, M. Xu, S. Lin, X. Shao, X. Zhang, Y. Liu, Y. Wang, Z. Chen and Y. Ma, *Nano Energy*, 2018, **51**, 489.
31 N. Kobayashi, H. Kuwae, J. Oshima, R. Ishimatsu, S. Tashiro, T. Imato, C. Adachi, S. Shoji and J. Mizuno, *J. Lumin.*, 2018, **200**, 19.
32 R. Kalthoum, M. Ben Bechir and A. Ben Rhaiem, *Phys. E*, 2020, **124**, 114235.
33 S. M. H. Qaid, B. A. Al-Asbahi, H. M. Ghaithan, M. S. AlSalhi and A. S. Al dwayyan, *J. Colloid Interface Sci.*, 2020, **563**, 426.
34 J. Tauc, in *Amorphous and Liquid Semiconductors*, ed. J. Tauc, Plenum Press, London and New York, 1974.
35 S. K. Gagandeep, B. S. Lark and H. S. Sahota, *Nucl. Sci. Eng.*, 2000, **134**, 208.
36 G. S. Shahane, B. M. More, C. B. Rotti and L. P. Deshmukh, *Mater. Chem. Phys.*, 1997, **47**, 263.
37 D. Bhattacharya, S. Chaudhuri and A. K. Pal, *Vacuum*, 1992, **43**, 313.
38 H. Rahmouni, M. Smari, B. Cherif, E. Dhahri and K. Khirouni, *Dalton Trans.*, 2015, **44**, 10457.
39 P. Maji, S. Chatterjee and S. Das, *Ceram. Int.*, 2015, **45**, 6012.
40 D. K. Pattanayak, R. K. Parida, N. C. Nayak, A. B. Panda and B. N. Parida, *J. Mater. Sci.: Mater. Electron.*, 2018, **29**, 6215.
41 D. K. Pradhan, P. Misra, V. S. Puli, S. Sahoo, D. K. Pradhan and R. S. Katiyar, *J. Appl. Phys.*, 2014, **115**, 243904.
42 A. Ray, A. Roy, S. De, S. Chatterjee and S. Das, *J. Appl. Phys.*, 2018, **123**, 104102.

43 Y. Mateyshina, A. Slobodyuk, V. Kavun and N. Uvarov, *Solid State Ionics*, 2018, **324**, 196.
44 A. Dhara, S. Sain, S. Das and S. K. Pradhan, *Mater. Res. Bull.*, 2018, **97**, 169.
45 T. Wang, J. Hu, H. Yang, L. Jin, X. Wei, C. Li, F. Yan and Y. Lin, *J. Appl. Phys.*, 2017, **121**, 084103.
46 C. R. Cena, A. K. Behera and B. Behera, *J. Adv. Ceram.*, 2016, **5**, 84.
47 C. G. Koops, *Phys. Rev.*, 1951, **83**, 121.
48 M. Ahmad, M. A. Rafiq, K. Rasool, Z. Imran and M. M. Hasan, *J. Appl. Phys.*, 2013, **113**, 043704.
49 P. Thongbai, S. Tangwancharoen, T. Yamwong and S. Maensiri, *J. Phys.: Condens. Matter*, 2008, **20**, 395227.
50 D. K. Rana, S. K. Singh, S. K. Kundu, S. Roy, S. Angappane and S. Basu, *New J. Chem.*, 2019, **43**, 3128.
51 P. Thongbai, S. Tangwancharoen, T. Yamwong and S. Maensiri, *J. Phys.: Condens. Matter*, 2008, **20**, 395227.
52 S. Patra, P. Sengupta, A. Ray, A. Roy and S. Das, *Ceram. Int.*, 2018, **44**, 14236.
53 J. Liu, C.-G. Duan, W.-G. Yin, W. N. Mei, R. W. Smith and J. R. Hardy, *J. Chem. Phys.*, 2003, **119**, 2812.
54 X. Z. Zuo, J. Yang, B. Yuan, D. P. Song, X. W. Tang, K. J. Zhang, X. B. Zhu, W. H. Song, J. M. Dai and Y. P. Sun, *J. Appl. Phys.*, 2015, **117**, 114101.
55 D. K. Rana, S. K. Singh, S. K. Kundu, S. Roy, S. Angappane and S. Basu, *New J. Chem.*, 2019, **43**, 3128.
56 P. Sengupta, P. Sadhukhan, A. Ray, R. Ray, S. Bhattacharyya and S. Das, *J. Appl. Phys.*, 2020, **127**, 204103.
57 B. E. Jun, H. K. Kim, Y. H. Hwang, B. C. Choi, J. H. Jeong, J. S. Bae and C. H. Kim, *J. Korean Phys. Soc.*, 2006, **49**, 2408.
58 D. K. Pradhan, P. Misra, V. S. Puli, S. Sahoo, D. K. Pradhan and R. S. Katiyar, *J. Appl. Phys.*, 2014, **115**, 243904.
59 N. Vol, *Nature*, 1977, **267**, 673.
60 M. Ben bechir and A. Ben Rhaiem, *Phys. E*, 2021, **130**, 114686.
61 M. Ben bechir and A. Ben Rhaiem, *Phys. E*, 2020, **120**, 114032.
62 M. Ben bechir and A. Ben Rhaiem, *J. Solid State Chem.*, 2021, **296**, 122021.
63 M. Ben Bechir, K. Karoui, M. Tabellout, K. Guidara and A. Ben Rhaiem, *J. Appl. Phys.*, 2014, **115**, 203712.
64 P. Maji, S. Chatterjee and S. Das, *Ceram. Int.*, 2019, **5**, 6012.
65 M. Ben Bechir, K. Karoui, M. Tabellout, K. Guidara and A. Ben Rhaiem, *J. Appl. Phys.*, 2014, **115**, 153708.